Thermoelectric oxide modules tested in a solar cavity-receiver

Petr Tomeš
Solid State Chemistry and Catalysis, Empa, Swiss Federal Laboratories for Materials Science and Research, CH-8600 Duebendorf, Switzerland

Clemens Suter
Department of Mechanical and Process Engineering, ETH Zurich, 8092 Zurich, Switzerland

Matthias Trottmann
Solid State Chemistry and Catalysis, Empa, Swiss Federal Laboratories for Materials Science and Research, CH-8600 Duebendorf, Switzerland

Aldo Steinfeld
Department of Mechanical and Process Engineering, ETH Zurich, 8092 Zurich, Switzerland; and Solar Technology Laboratory, Paul Scherrer Institute, 5232 Villigen, Switzerland

Anke Weidenkaff[a)]
Solid State Chemistry and Catalysis, Empa, Swiss Federal Laboratories for Materials Science and Research, CH-8600 Duebendorf, Switzerland

(Received 8 December 2010; accepted 15 April 2011)

Four-leg thermoelectric oxide modules (TOMs) consisting of two p-type ($La_{1.98}Sr_{0.02}CuO_4$) and two n-type ($CaMn_{0.98}Nb_{0.02}O_3$) thermoelectric (TE) legs were produced with a manufacturing quality factor between 30 and 60%. The pressed sintered TE legs revealed 90% of the theoretical density to ensure a sufficient mechanical stability of the TE modules. The legs were connected electrically in series and sandwiched thermally in parallel between two Al_2O_3 plates serving as absorber and cooler, respectively. A solar cavity-receiver packed with an array of TOMs was subjected to concentrated thermal radiation with peak solar radiative flux intensities exceeding 600 kW/m^2. Temperature distributions in the cavity, open-circuit voltage (V_{OC}), and maximum output power ($P_{\max}$) were measured for different external loads and solar radiative fluxes (q_{in}). Finally, the solar-to-electricity conversion efficiency (η) was calculated.

I. INTRODUCTION

Oxide materials are promising candidates for high-temperature thermoelectric (TE) applications. In contrast to conventional TE materials based on Bi_2Te_3, which are toxic and have limited chemical stability above $T \sim 523$ K in air, they are temperature-stable, oxidation-resistant, and nontoxic.[1–4] Oxide materials, especially with perovskite-type structure, can be easily synthesized with controllable composition and TE properties.[5–8] The low costs of these materials are beneficial as well. The advantage of Bi_2Te_3-based TE materials is the better performance[9,10] expressed by the figure-of-merit, $ZT = S^2T/\rho\kappa$, where S is the Seebeck coefficient, ρ is the electrical resistivity, and κ is the thermal conductivity.[11]

The maximum conversion efficiency is thermodynamically limited by the Carnot efficiency.[12] The performance and conversion efficiency of TE modules depend not only on the properties but also on the compatibility factors of the used TE materials, on the geometrical factors of the TE module, and on the quality of the electrical and thermal contacts.[11,13,14] The direct conversion of solar irradiation into electricity at high temperatures has recently been experimentally demonstrated.[15] A heat transfer analysis of directly irradiated TE modules has shown that 60% of the incident solar radiation is lost by reradiation.[16] Reradiation can be significantly reduced by utilizing a solar cavity-receiver.

The objective of the work presented in this article is to show the potential of thermoelectric oxide modules (TOMs) for the direct conversion of solar heat into electrical energy as possible low-maintenance alternative to conventional technologies. To proof this concept, a series of perovskite-type TOMs were placed in a solar cavity-receiver, which is aimed at reducing reradiation and thereby enhancing the conversion efficiency of the TOMs.[16] TOMs were measured individually and connected in series at different radiation levels in terms of the resulting temperature distribution in the cavity, open-circuit voltage, and maximum output power at different external loads. Finally, the conversion efficiency is evaluated.

II. EXPERIMENTAL

The TE legs consisted of synthesized $La_{1.98}Sr_{0.02}CuO_4$ (p-type)[17] and $CaMn_{0.98}Nb_{0.02}O_3$ (n-type).[6] Both materials

---

[a)] Address all correspondence to this author.
e-mail: anke.weidenkaff@empa.ch

DOI: 10.1557/jmr.2011.125

were prepared by a *chimie douce* synthesis procedure described in previous publications[5] and literature cited herein. The calcined powders of $La_{1.98}Sr_{0.02}CuO_4$ and $CaMn_{0.98}Nb_{0.02}O_3$ were characterized by x-ray diffraction (XRD).[6,17] The particle size was reduced to the 1–6 μm by ball milling the phase pure powders. Subsequently, the powders were pressed into disc-shaped pellets with a diameter of 32 mm using a hydrostatic press. Both p- and n-type pellets were sintered for 5 h at 1373 K and for 5 h at 1523 K, respectively. The final p- and n-type legs with a length of $L \sim 5.0$ mm and a cross-sectional area of $A \sim 5.5 \times 5.5$ mm^2 were obtained by grinding and cutting the pellets.

The electrical resistivity and the Seebeck coefficient were measured in air with a RZ2001i Ozawa Science measurement system (Nishiki, Japan) in the temperature range of 300 K $< T <$ 950 K. The thermal conductivity was evaluated indirectly by separate measurements of the thermal diffusivity in a laser flash apparatus (Netzsch LFA, Burlington, MA) and the specific heat by a differential scanning calorimeter (Netzsch DSC, Burlington, MA).[8]

A series of four-leg TOMs were assembled by connecting the p- and n-type TE legs electrically in series and thermally in parallel between two electrically insulated and thermally conductive Al_2O_3 plates (Rubalit 708 S, CeramTec GmbH, Plochingen, Germany) with a cross-section of 25 × 25 mm^2 and a thickness of 0.5 mm.[18] The assembly drawing is shown in Fig. 1. The electrical contacts between the TE legs and the Al_2O_3 plates were made by a two-step metallization process using two types of conductor paste chosen based on previous experimental observations. The first step was a two-layer screen-printing[19] through a stainless steel stencil to obtain an efficient metallization of the Al_2O_3 surface. This process was applied to both the surface of the TE legs and the Al_2O_3 plates. The first metal layer was provided by printing with 4597 AuPtPd conductor paste (DuPont, Wilmington, DE) to obtain a conductive surface, which is especially important on the electrically insulating Al_2O_3 plates. The AuPtPd-coated TE legs and Al_2O_3 plates were dried at 423 K for 15 min to evaporate the solvents, followed by annealing at 1223 K for 15 min to induce the diffusion. AuPtPd conductor paste embodied a strong adhesion on the Al_2O_3 surface. A second conductive layer was applied using a AgPd conductor paste (DuPont) and the same drying and annealing processes as described above. In a second step, a Ag sheet was placed between the TE legs and the Al_2O_3 plates on both, the hot and the cold sides of the TOMs serving as the electrical contacts. Several screening experiments revealed an improved connection of the Ag electrical contacts on an AgPd metal layer. Finally, the Al_2O_3 cover plates were attached and all components assembled (Fig. 1). The modules were heated at 1223 K for 1 h to solder the conductive layers and to ensure and test the thermal stability. The Al_2O_3 plate surface on the irradiated side was coated with a homogeneous graphite layer to increase the absorption of solar radiation.[20]

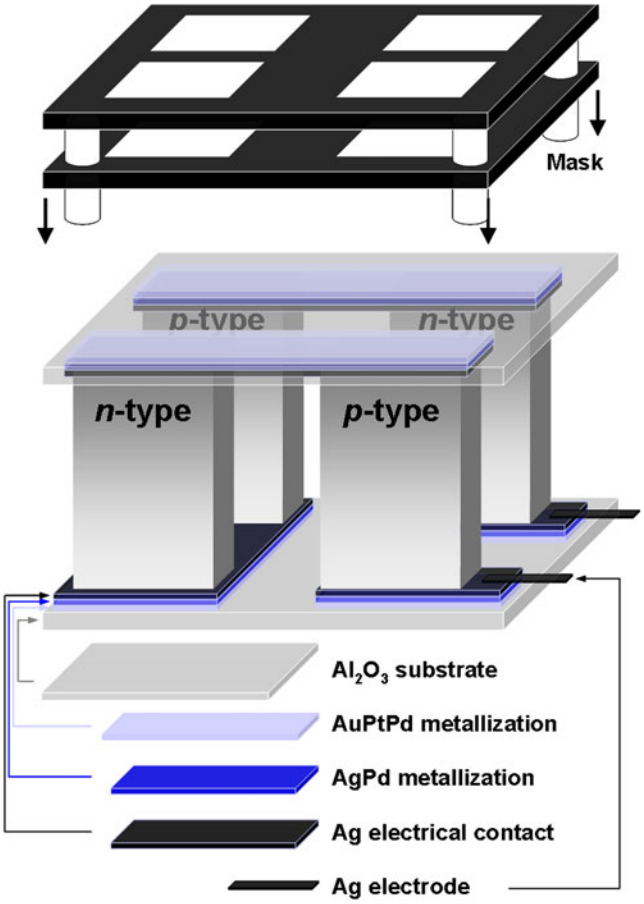

FIG. 1. Assembly drawing of a thermoelectric oxide module.

The performance of all TOMs was tested with a test unit: the open-circuit voltages were measured, and the maximum output power and the total resistance were evaluated. The current-voltage characteristic was recorded measuring the voltage at different external loads (Höcherl & Hackl DC load ZS 506-4 550 Watt, Konzell, Germany).[21] The measurements were monitored using the LABVIEW software (National Instruments, Austin, TX).[22] The output power was deduced from the current–voltage curve.[18] The hot side of the TOM was heated by a heater, and the cold side was cooled by a water-cooled Cu block. TOMs were attached to the Cu cooling block using a thermally conductive paste (DuPont) to guarantee a good heat transfer from the cold Al_2O_3 plate to the Cu cooling block. During the measurement, a pressure load of 80 kN·m^{-2} was applied to increase the heat transfer and to minimize the thermal resistance between the heater and the hot plate. The temperature on the hot and the cold sides of TOMs was measured using two K-type thermocouples.

The TOMs were tested in a solar cavity-receiver for their ability to convert solar radiation generated by a high-flux solar simulator (HFSS)[23] into electrical energy.

The radiative flux peaks in function of the HFSS arc were measured by a Thermogage Circular Foil Flux Transducer TG1000-1 (Sequoia Technology Ltd, Reading, UK) (accuracy ±3%) placed in the center of the focal plane. The radiative flux distribution was measured optically on an Al_2O_3-plasma-coated Lambertian target with a CCD camera equipped with optical filters and calibrated with a Kendall radiometer (error of ±8%). The flux measurement showed a quasi constant distribution within the aperture size of 20×81 mm^2. Radiation losses in the compound parabolic concentrator (CPC) were estimated by a three-dimensional simulation of the HFSS, the CPC, and the cavity using a Monte-Carlo ray-tracing program.[24] Assuming a CPC mirror reflectivity of 0.8 and a mirror reflection of 95%, losses of ~33.3% were simulated.

A sketch of a solar cavity-receiver designed for 18 TOMs is shown in Fig. 2. The rectangular shape of the solar cavity-receiver contains inlets and outlets for an encapsulated circulating water cooling system. The rectangular aperture for the incidence of concentrated solar radiation is at the top of the solar cavity-receiver. The integral water-cooled CPC has the function to enhance the radiative flux by a factor of 1.4 and to provide a uniform irradiation of the TE modules. This is crucial to realize equal temperature differences across each module. Besides the above-mentioned quality of the electrical and thermal contacts, the performance and conversion efficiency also depend on the packing quality of the TE modules inside the solar cavity-receiver including the lateral insulation of the TOM array (18 pcs.). All electric wires were connected at a pinboard allowing the connection to be switched from parallel (measurement of individual TOMs) to serial connection circuit (measurement of serial connected TOMs). An efficient thermal contact between the TOMs and the cooler of the solar cavity-receiver was provided by a thermal conduction paste (DuPont) and by a special clamping mechanism containing springs and ribbons (Fig. 2). The temperature on the hot side was monitored and controlled to avoid that the temperature in the cavity exceeds the melting point of Ag (T ~1235 K) used in TOMs.[25]

III. RESULTS AND DISCUSSION

The p- and n-type TE materials were hydrostatically pressed into pellets. They showed 90% of the theoretical density without any crack formation due to the uniformly applied pressure. The p- and n-type materials have thermal conductivities of 2.5 W·m^{-1} K^{-1} and 3 W m^{-1}·K^{-1} above 300 K, respectively. Bocher et al.[7] measured a by 0.78 W·m^{-1}·K^{-1} lower thermal conductivity above 300 K for the n-type material. The difference can be attributed to modified synthesis conditions. For our case denser TE legs with better mechanical properties but different microstructure were obtained. A shorter sintering time and a lower sintering temperature (T = 1473 K) resulted in samples with different morphology and microstructure and lower theoretical density (80.77%). This result highlights that further research on the relation/trade-off between thermal conductivity and mechanical stability of the TE materials is needed to improve the thermal properties in high-temperature applications.

Similar TE properties of the p- and n-type TE materials are a prerequisite for good conversion efficiencies of TOMs as was described previously by Snyder et al.[13] The compatibility factor s, defined as $s = [(1 + ZT)^{1/2} - 1]/ST$ is

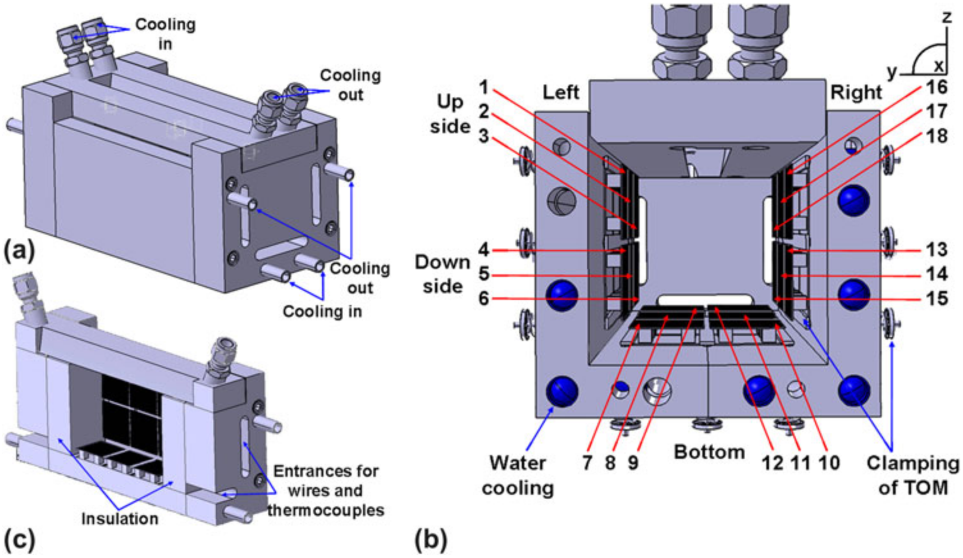

FIG. 2. Design of a solar cavity-receiver packed with 18 TOMs. (a) Exterior view containing the cavity and the compound parabolic concentrator, and (b) cross-sectional view and (c) longitudinal view of a solar cavity-receiver.

used to assess the similarity of the TE properties of different materials. For maximum conversion efficiencies at large temperature gradients, the compatibility factor should not vary much with temperature. The p-type ($La_{1.98}Sr_{0.02}CuO_4$) and the n-type ($CaMn_{0.98}Nb_{0.02}O_3$) leg materials were selected from candidate materials with regard to most suitable compatibility factors to maximize the conversion efficiency and enhance the output power.[13,15] Both materials have similar metallic electrical resistivities of $\rho_p = 24$ mΩ·cm and $\rho_n = 20$ mΩ·cm at $T = 300$ K, respectively. Both materials exhibit large absolute thermopower values ($S_p = +200$ $\mu V \cdot K^{-1}$ and $S_n = -160$ $\mu V \cdot K^{-1}$) at $T = 300$ K. The figure-of-merit ZT for the p- and n-type materials was published previously.[15] The compatibility factors of both materials are perfectly matching around $T = 425$ K but differ by a factor of 1.3 at $T = 500$ K and by a factor of 2.3 at $T = 800$ K. This implies a decrease of the conversion efficiency of the four-leg TOMs at high-temperature gradients.

Figure 3(a) shows the geometrical parameters (cross-section and length) of the p- and n-type legs for all 18 modules. The TE area of two p- and two n-type legs (A) varies in the range of 121.3 $mm^2 < A <$ 126.3 mm^2 and the TE leg length (L) in the range of 4.95 mm $< L <$ 5.15 mm. The variability is a consequence of the production process of the p- and n-type pellets (see "Experimental"). The maximum output powers (P_{max}), inverse total resistances (R_{total}^{-1}), and open-circuit voltages (V_{OC}) for all TOMs are plotted in Fig. 3(b).

The corresponding temperatures on the hot side (T_{hot}) and the cold side (T_{cold}) of the TOMs were achieved using the heater and the water-cooled Cu block. T_{hot} and T_{cold} varied in the range of 680 K $< T_{hot} <$ 738 K and 338 K $< T_{cold} <$ 388 K, respectively, due to the position inaccuracy of the thermocouples. P_{max} varies in the range of 0.048 W $< P_{max} <$ 0.081 W and V_{OC} in the range of 0.349 V $< V_{OC} <$ 0.420 V. The variation of P_{max} can be associated with the TOM's total resistances, which vary in the range of 0.48 Ω $< R_{total} <$ 0.79 Ω. Figure 3(b) reveals that the progression of R_{total}^{-1} and P_{max} coincide. The diversity of the total resistance is mainly due to different contributions of the contact resistances (R_{cont}), which are not negligible in a TOM.[14] The different contact resistances are a consequence of the manufacturing method of the TOMs. In comparison, the material resistances (R_{mater}) originating from small differences in the geometry of the p- and n-type TE legs do only make a minor contribution to the total resistances. R_{mater} can be calculated from the temperature difference across the TE legs and the temperature-dependent electrical resistivity of the p- and n-type TE legs. This parameter is important for the determination of the contact resistance and the device quality [manufacturing quality factor (MQF)] associated with manufacturing defects according to the following equation: $MQF = R_{mater}/R_{total}$. The thermal contacts were not directly taken into account, but they are one of the parts influencing the MQF. The MQFs of all TOMs are in the range of $0.3 < MQF < 0.6$, which is comparable to other published TOMs.[26] The slight scattering of the open-circuit voltages is most probably due to inconsistencies of the thermal contacts between the Al_2O_3 plates and the cooler and heater, respectively.

TE module failures are caused by degradation due to either changes in the TE material properties (sublimation of material, oxygen loss, crack formation due to thermal stress) or an increase in the electrical contact resistance, especially at high temperatures, mainly caused by compositional and structural changes in the vicinity of junctions. Therefore, one selected TOM was exposed to a temperature of ~800 K measured at the heater for 65 h in air (Fig. 4). Relevant module parameters were measured at regular intervals. The maximum temperature gradient across the TOM ($\Delta T = T_{heater} - T_{cold}$ $side_{TOM}$), where T_{cold} $side_{TOM}$ is the temperature on the Al_2O_3 plate on the cold side of the TOM, is a good module stability indicator. In the course of the experiment, an average gradient of

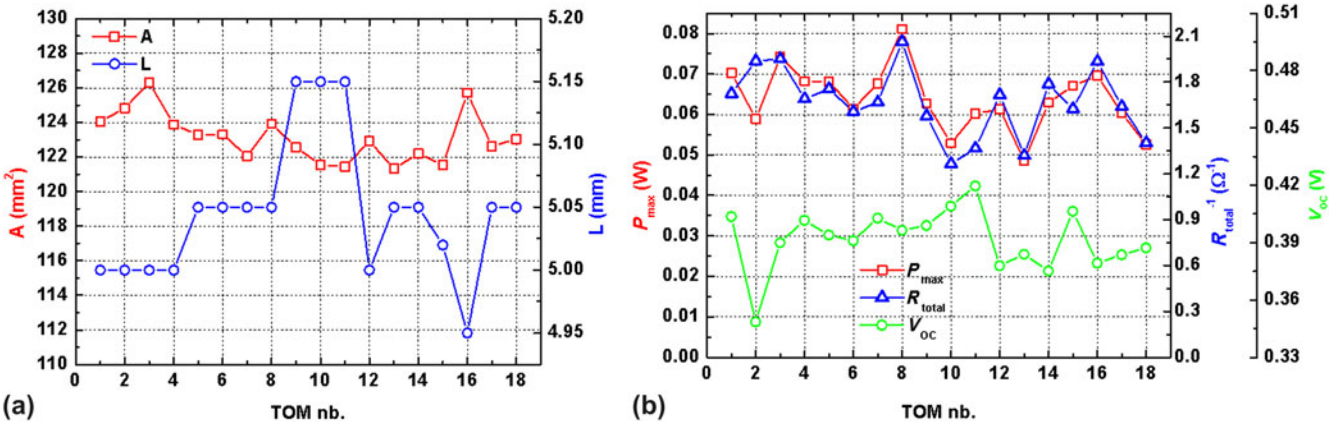

FIG. 3. (a) Cross-sectional area and length of the p- and n-type thermoelectric legs. (b) Maximum output power (P_{max}), inverse total resistance (R_{total}^{-1}), and open-circuit voltage (V_{OC}) of all TOMs measured by applying heat by means of a heating plate.

ΔT = 344.55 K with a standard deviation of σ = 0.56 K was determined. Other important parameter reflecting the stability of the TE materials is the open-circuit voltage. During the 65-h observation period, the open-circuit voltage was V_{OC} = 0.3870 V with $\sigma = 3.6\ 10^{-4}$ V. Expressed in percent, the standard deviation σ is small, suggesting that the TE materials are degradation-resistant.

Figure 5 shows the average open-circuit voltages (V_{OC}) of the modules with either uncoated or graphite-coated Al_2O_3 absorber plates depending on their position in the solar cavity-receiver (bottom, upper side, and lower side). The plots reveal the highest V_{OC} for TOMs at the receiver bottom irrespective of the surface coating. At an incident heat flux of q_{in} = 62 W·cm^{-2}, open-circuit voltages were V_{OC} = 0.261 V and V_{OC} = 0.388 V for uncoated [Fig. 5(a)] and graphite-coated [Fig. 5(b)] TOMs at the receiver bottom, respectively. The (horizontal) errors of the incoming heat flux are due to inaccurate positioning of the solar cavity-receiver (±2.5 mm), leading to deviations between 10.8% ± 11.8%. The (vertical) errors of the open-circuit voltage are due to the averaging the measurement results of several TOMs and experiments. To obtain the same open-circuit voltage at the bottom with the uncoated compared to the graphite-coated TOM, an incident heat flux of q_{in} = 99.8 W·cm^{-2} has to be applied. Both uncoated and graphite-coated TOMs located at the upper or lower sides of the receiver had lower open-circuit voltages.

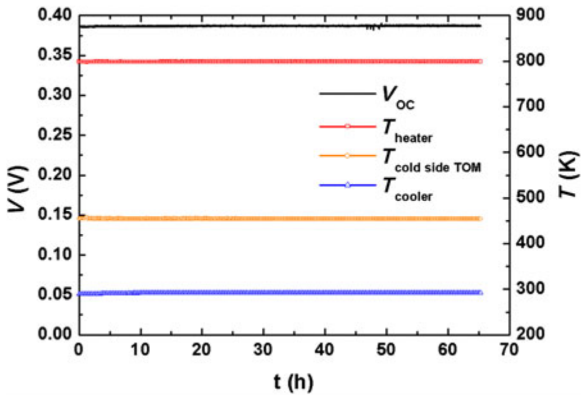

FIG. 4. Long-term measurement of TOM17 showing the progression of the open-circuit voltage and the temperatures on the heater, the cooler, and the cold (T_{cold}) Al_2O_3 plates.

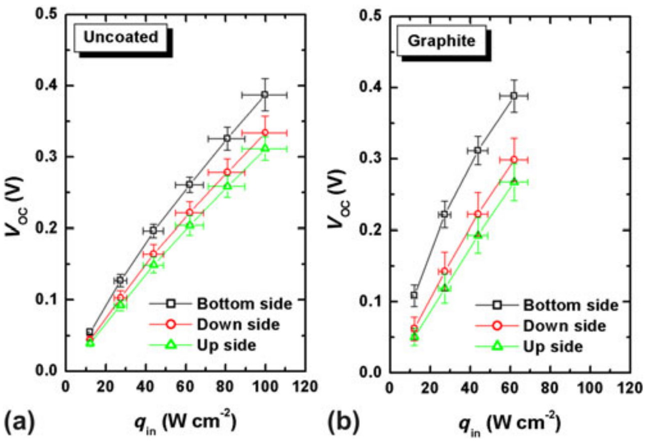

FIG. 5. Average open-circuit voltages (V_{OC}) of (a) uncoated and (b) graphite-coated TOMs, in dependence of their position in the solar cavity-receiver (bottom, lower side, and upper side).

Maximum output powers (P_{max}) of 10 graphite-coated TOMs are plotted in Fig. 6(a), and the maximum temperature T_{max} (recorded at TOM11) against time is shown in Fig. 6(b). The red numbered labels in Fig. 6(b) indicate the steady-state regions of the maximal temperature T_{max}, specified below. In the steady-state regions, T_{max} [shown in Fig. 6(b)] and V_{OC} were evaluated and P_{max} was calculated. As expected, P_{max} decreases in the order: receiver bottom (TOM8, TOM11, TOM7, and TOM10) > lower side wall (TOM14, TOM4, and TOM6) > upper side wall (TOM2, TOM18, and TOM16), which is indicated by the arrow in Fig. 6(a).

However, this pattern changes for the graphite-coated TOMs at an incident heat flux of q_{in} >70 W·cm^{-2} and a maximum temperature of T_{max} >858 K (recorded at TOM11) because of partial decomposition of the graphite layer (red dashed line). This process of the partial decomposition of the graphite layer starts at the TOMs at the receiver bottom (TOM8, TOM11, TOM7, and TOM10), resulting in a "saturation" of P_{max}, as it is shown for TOM8 in Fig. 6(a). The possible solutions of the decomposition of the graphite layer could be the sealing of the solar cavity-receiver or exchanging the absorber layer by another material with similar thermal conductivity as Al_2O_3 and comparable emissivity as graphite. Nevertheless, the highest P_{max} = 0.1 W was recorded for the module TOM8 at q_{in} = 99.8 W·cm^{-2}.

Output power and current–voltage curves for uncoated and coated TOMs connected in series are plotted in Fig. 7. The maximum temperature T_{max} is stated below the graphs. The maximum generated voltage for uncoated and coated TOMs is 6.0 V at T_{max} = 833 K and 7.7 V at T_{max} = 885 K, respectively.

The maximum output power and total resistance of the TOMs were determined from the output power/voltage/current characteristics in Fig. 7. The conversion efficiency was calculated according to $\eta = P_{max}/(q_{in} \cdot S_{CPC})$, where S_{CPC} is the entry surface of the CPC. The maximum output power, the total resistance, and the conversion efficiency of coated and uncoated TOMs are plotted in Fig. 8. The maximum output power of P_{max} ~1.42 W was achieved for the coated TOMs connected in series [Fig. 8(b)]. The total resistance R_{total} was slightly higher for coated TOMs than for uncoated TOMs because of a higher T_{max} (Fig. 7) and increases with increasing heat flux from R_{total} = 8.48 Ω and R_{total} = 8.91 Ω at q_{in} = 12.03 W·cm^{-2} to R_{total} = 9.77 Ω

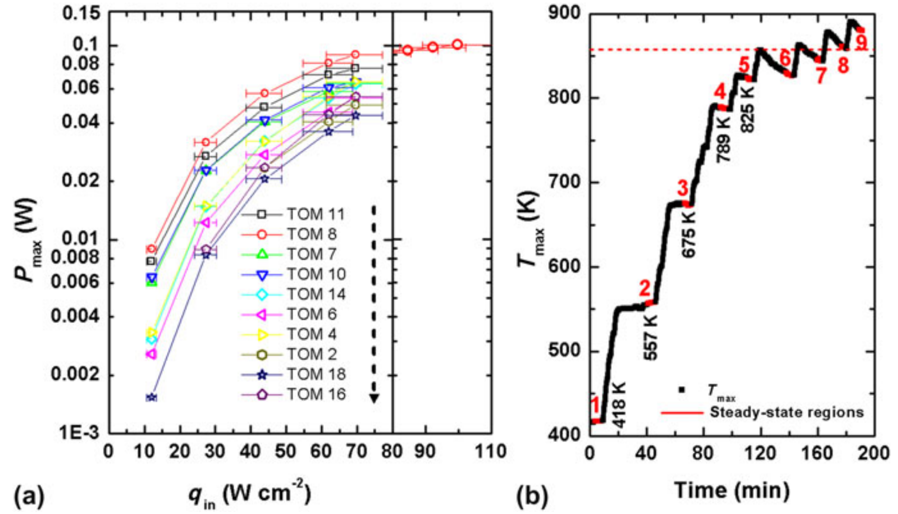

FIG. 6. (a) Maximum output power (P_{max}) of 10 individually measured graphite-coated TOMs. (b) Temperature (T_{max}) recorded on the hot side of TOM11; the red numbered labels indicate the steady-state regions of T_{max}.

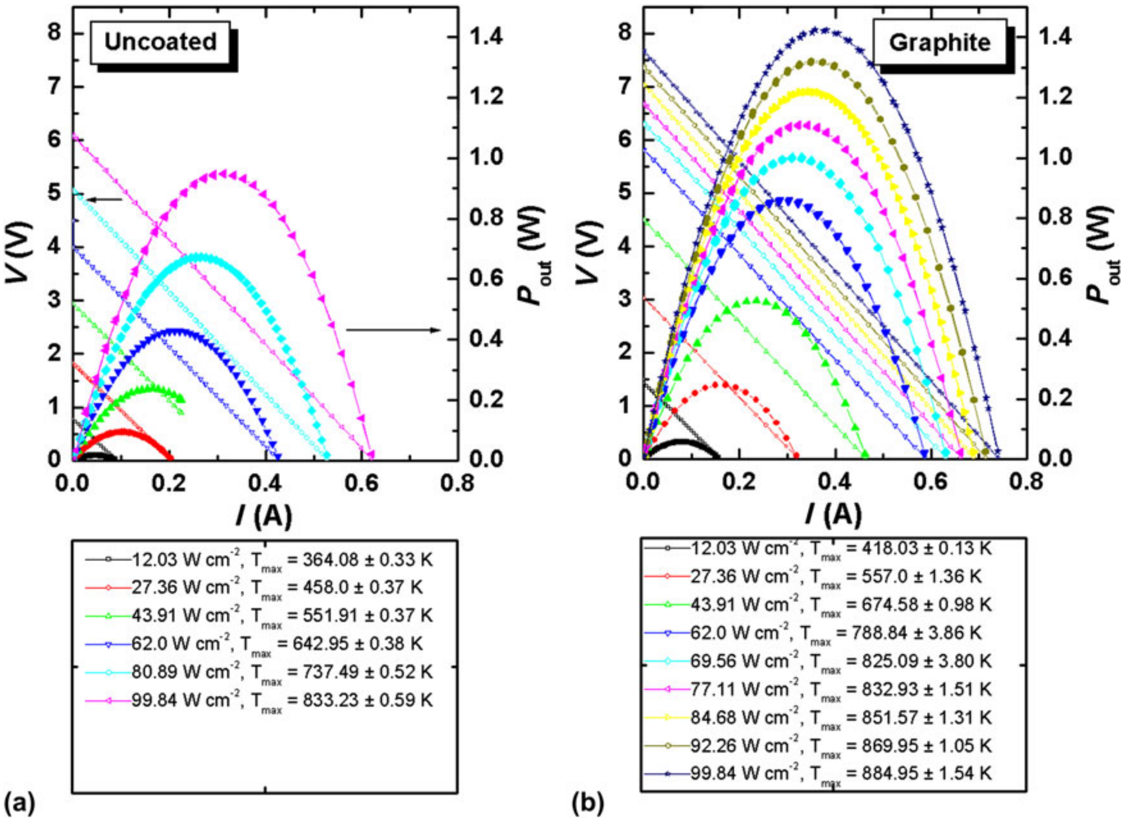

FIG. 7. Output power and voltage (V) versus current (A) at different heat fluxes of (a) graphite-coated and (b) uncoated TOMs. T_{max} is specified in all cases.

and R_{total} = 10.0 Ω at q_{in} = 99.8 W·cm^{-2} for uncoated and coated TOMs, respectively. This is mainly attributed to an increase in the contact resistance R_{cont} and in the material resistance of the TE legs due to the metallic properties, as previously shown.[15] The conversion efficiency of the graphite-coated TOMs was already saturated at q_{in} = 77.11 W·cm^{-2} and T_{max} >858 K. The conversion efficiency increases with increasing heat fluxes up to η ~0.08% and η ~0.13% at q_{in} = 99.8 W·cm^{-2} for uncoated and graphite-coated TOMs, respectively. By comparison, in a previous experiment, a single graphite-coated TOM subjected to direct concentrated irradiation only had a maximum conversion

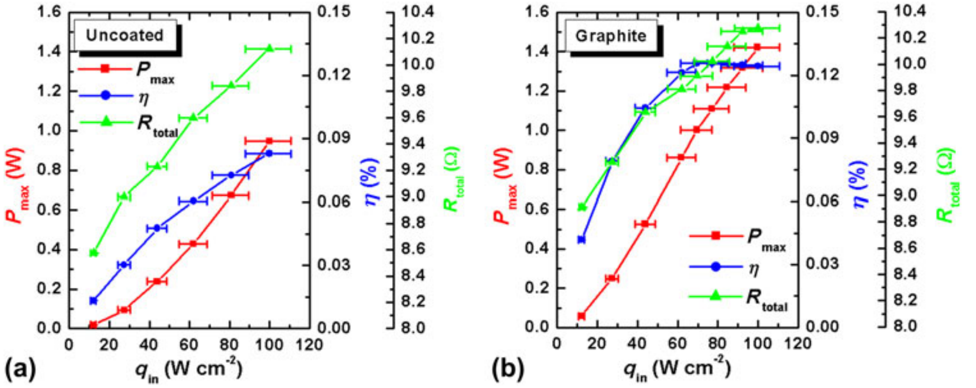

FIG. 8. Maximum output power (P_{max}), total resistance (R_{total}), and conversion efficiency (η) of (a) uncoated and (b) graphite-coated TOMs electrically connected in series.

efficiency of η ~0.08%.[15] This implies an efficiency improvement of ~62%.

IV. CONCLUSIONS

A series of TOMs with $0.3 < MQF < 0.6$, containing $La_{1.98}Sr_{0.02}CuO_4$ as p-type and $CaMn_{0.98}Nb_{0.02}O_3$ as n-type TE material, were successfully fabricated and used to convert concentrated solar radiation into electrical energy by using concentrated thermal radiation as energy source. The TE materials were chosen based on best compatibility factors and not on TE activity. In a long-term measurement (65 h) of one selected TOM, performance stability at high temperatures was proven. A solar cavity-receiver packed with an array of TOMs was constructed to efficiently capture concentrated solar radiation and to reduce losses due to reradiation. Open-circuit voltage V_{OC} and maximum output power P_{max} of each TOM was measured individually showing the highest V_{OC} and P_{max} for TOMs located at the bottom of the cavity. Due to the higher absorptivity of graphite, V_{OC} and P_{max} were expected to be higher for coated than for uncoated TOMs at the same incoming solar power q_{in}, which was confirmed by the measurements. The maximum generated voltage for coated TOMs connected in series was $V_{OC} = 7.7$ V at $T_{max} = 885$ K. The total resistance increased with increasing heat flux mainly due to an increase in the contact resistance R_{cont} and in the material resistance of the TE legs arising from the material's metallic nature. A maximum output power of P_{max} ~1.42 W and a solar-to-electricity conversion efficiency of η ~0.13% was achieved for the coated TOMs, which is an improvement of ~62% compared to a single graphite-coated TOM subjected to direct solar irradiation.

ACKNOWLEDGMENTS

We thank the Swiss Federal Office of Energy and Swiss National Foundation for financial support and O. Brunko, D. Alfarug, and U. Gfeller for their help with the synthesis.

REFERENCES

1. E.S. Reddy, J.G. Noudem, S. Hebert, and C. Goupil: Fabrication and properties of four-leg oxide thermoelectric modules. *J. Phys. D: Appl. Phys.* **38**, 3751 (2005).
2. W. Shin, N. Muruyama, K. Ikeda, and S. Sago: Thermoelectric power generation using Li-doped NiO and (Ba, Sr)PbO_3 module. *J. Power Sources* **103**, 80 (2001).
3. R. Funahashi, M. Mikami, T. Mihara, S. Urata, and N. Ando: A portable thermoelectric-power-generating module composed of oxide devices. *J. Appl. Phys.* **99**, 066117 (2006).
4. R. Funahashi, I. Matsubara, H. Ikuta, T. Takeuchi, U. Mizutani, and S. Sodeoka: Oxide single crystal with high thermoelectric performance in air. *Jpn. J. Appl. Phys.* **39**, 1127 (2000).
5. A. Weidenkaff: Preparation and application of nanostructured perovskite phases. *Adv. Eng. Mater.* **6**, 709 (2004).
6. L. Bocher, R. Robert, M.H. Aguirre, S. Malo, S. Hébert, A. Maignan, and A. Weidenkaff: Thermoelectric and magnetic properties of perovskite-type manganate phases synthesised by ultrasonic spray combustion (USC). *Solid State Sci.* **10**, 496 (2008).
7. L. Bocher, M.H. Aguirre, D. Logvinovich, A. Shkabko, R. Robert, M. Trottmann, and A. Weidenkaff: $CaMn_{1-x}Nb_xO_3$ ($x \leq 0.08$) perovskite-type phases as promising new high-temperature n-type thermoelectric materials. *Inorg. Chem.* **47**, 8077 (2008).
8. M.H. Aguirre, S. Canulescu, R. Robert, N. Homazava, D. Logvinovich, L. Bocher, T. Lippert, M. Döbeli, and A. Weidenkaff: Structure, microstructure, and high-temperature transport properties of $La_{1-x}Ca_xMnO_{3-\delta}$ thin films and polycrystalline bulk materials. *J. Appl. Phys.* **103**, 013703 (2008).
9. S.S. Kim, F. Yin, and Y. Kagawa: Thermoelectricity for crystallographic anisotropy controlled Bi–Te based alloys and p–n modules. *J. Alloy. Comp.* **419**, 306 (2006).
10. O. Yamashita and S. Sugihara: High-performance bismuth-telluride compounds with highly stable thermoelectric figure of merit. *J. Mater. Sci.* **40**, 6439 (2005).
11. D.M. Rowe: *Thermoelectrics Handbook: Macro to Nano* (Taylor & Francis Group, Boca Raton, FL, 2006), pp. 1–5.
12. J. Yang and T. Caillat: Thermoelectric materials for space and automotive power generation. *MRS Bull.* **31**, 224 (2006).
13. G.J. Snyder: Application of the compatibility factor to the design of segmented and cascaded thermoelectric generators. *Appl. Phys. Lett.* **84**, 2436 (2004).
14. S.A. Omer and D.G. Infield: Design optimization of thermoelectric devices for solar power generation. *Sol. Energy Mater. Sol. Cells* **53**, 67 (1998).
15. P. Tomeš, C. Suter, M. Trottmann, M.H. Aguirre, P. Haueter, A. Steinfeld, and A. Weidenkaff: Thermoelectric oxide modules

(TOMs) applied in direct conversion of simulated solar radiation into electrical energy. *Materials* **3**, 2801 (2010).

16. C. Suter, P. Tomeš, A. Steinfeld, and A. Weidenkaff: Heat transfer and geometrical analysis of thermoelectric converters driven by concentrated solar radiation. *Materials* **3**, 2735 (2010).
17. S. Zhou, J. Zhao, S. Chu, and L. Shi: Synthesis, characterization and magnetic properties of lightly doped $La_{2-x}Sr_xCuO_4$ (x = 0.04) nanoparticles. *Physica C* **451**, 38 (2007).
18. P. Tomeš, R. Robert, M. Trottmann, L. Bocher, M.H. Aguirre, J. Hejtmánek, and A. Weidenkaff: Synthesis and characterization of new ceramic thermoelectrics implemented in a thermoelectric oxide module. *J. Electron. Mater.* **39**, 1696 (2010).
19. D.D.L. Chung: *Composite Material: Science and Applications (Engineering Materials and Processes)*, 2nd ed. (Springer-Verlag, London, England, 2010), p. 246.
20. M.A. Bramson: *Infrared Radiation: A Handbook of Applications* (Plenum Press, New York, NY, 1968).
21. http://www.hoecherl-hackl.com/geraetedocs/E_technischeDaten_ZS.php?gername=ZS506-4.
22. http://www.cord.edu/faculty/jensen/LabVIEW/index.htm.
23. D. Hirsch, P.V. Zedtwitz, T. Osinga, J. Kinamore, and A. Steinfeld: A new 75 kW high-flux solar simulator for high-temperature thermal and thermochemical research. *J. Sol. Energy Eng.* **125**, 117 (2003).
24. J. Petrasch: Thermal modeling of solar chemical reactors: transient behavior, radiative transfer (Master thesis, ETH, Zurich, Switzerland, 2002).
25. M. Bauccio: *ASM Metals Reference Book*, 3rd ed. (ASM International, Materials Park, OH, 1997), p. 139.
26. S. Lemonnier, Ch. Goupil, J. Noudem, and E. Guilmeau: Four-leg $Ca_{0.95}Sm_{0.05}MnO_3$ unileg thermoelectric device. *J. Appl. Phys.* **104**, 014505 (2008).